Soft Matter

PAPER

View Article Online
View Journal | View Issue

Check for updates

Cite this: *Soft Matter*, 2022, **18**, 4464

Formation of colloidal chains and driven clusters with optical binding†

Dominique J. Davenport * and Dustin Kleckner

Received 28th March 2022,
Accepted 26th May 2022

DOI: 10.1039/d2sm00393g

rsc.li/soft-matter-journal

We study the effects of the optical binding force on wavelength sized colloidal particles free to move in a counter-propagating beam. This work is motivated by the concept of using optical binding to direct the assembly of large numbers of colloidal particles; previous work has used small numbers of particles and/or 1D or 2D restricted geometries. Utilizing a novel experimental scheme, we describe the general static and dynamic self-organization behaviors for 20–100 particles free to move in 3-dimensional space. We observe the self-organization of the colloids into large optically bound structures along with the formation of driven particle clusters. Furthermore we show that the structure and behavior of these optically bound systems can be tuned using the refractive index of the particles and properties of the binding light. In particular, we show that the driven behavior originates from *N*-body interactions, which has significant implications for future work on optically bound clusters of more than 2 particles.

Published on 31 May 2022. Downloaded by University of California - Merced on 9/2/2022 6:50:10 PM.

1 Introduction

Self-organization is the spontaneous formation of structure *via* the interactions of their constituent particles.[1] The resulting structures from a self-organized system can be found in equilibrium and non-equilibrium states; the latter provides a pathway towards active and adaptive matter. While adaptive materials are common in living systems such as cells, it is possible to artificially introduce dynamic forces which can externally deliver energy to a system while mediating self-organization.[2] Dynamic self-organization is relatively new but active field of self-assembly with the goal of extending our knowledge of equilibrium thermodynamics onto living systems. Some examples include the dynamic assembly of non-biological components including active colloids,[3–5] rotating discs,[6,7] and magnetic swimmers.[8–10]

Optical binding is a long-range light-induced force which causes dielectric particles to interact mutually through light-scattering.[11] In theory, optical binding can be felt between polarizable molecules ($\sim$1 nm)[12] up to biological cells[13] ($\sim$5 μm). In practice, because the force is relatively weak and requires a strong scattering response, the effects of optical binding are observed most strongly for objects that are on the order of the wavelength of light in size. Moreover, optical binding can give rise to non-equilibrium forces because the optical field applied to the system is also a constant supply of external momentum which can contribute to particle motion,[14] although this effect has been largely unexplored in previous experimental work. In principle optical binding forces can be explained using existing approaches – forces can be exactly predicted using a multiple scattering calculations – but nonetheless it remains difficult to predict and explain the behavior of systems composed of many particles.[14]

Numerous past studies have illustrated the complexity of the optical binding force. Two-particle studies have shown that the force can contain multiple stable points defined by multiples of the light wavelength.[11,15,16] By increasing the number of particles, previous experimental and computational studies have shown the self-organization of 1-dimensional chains,[17] static and drifting 2-dimensional lattices exhibiting stable and quasi-stable behaviors,[18] and observations of bistability[19] and multistability[20] in the equilibrium positions of optically bound particles.[21] The complexity that arises from optical binding in multi-particle systems can largely be attributed to feedback in the form of interference with the incoming field through multiple scattering effects.[21] One often neglected fact is that optical binding forces are sensitive to *N*-body effects, and can not be treated as strictly pairwise interactions.[22] These *N*-body interactions can lead to highly correlated and emergent behaviors but can consequently be difficult to model. More recent studies have described complex dynamical assemblies of metallic and dielectric nanoparticles.[23–25] These studies suggest that highly nonlinear and dynamic interactions can occur for smaller particles, where interactions are highly pair-wise, because of the complexity of the potential landscapes generated by optical scattering alone.[26] The presence of thermal noise in a complex potential landscape can disrupt stability. Thus, in studying a system which *N*-body forces may be strong and potential

5200 North Lake Rd., Merced, California, 95343, USA.
E-mail: ddavenport3@ucmerced.edu, dkleckner@ucmerced.edu

† Electronic supplementary information (ESI) available. See DOI: https://doi.org/10.1039/d2sm00393g

This journal is © The Royal Society of Chemistry 2022

Published on 31 May 2022. Downloaded by University of California - Merced on 9/2/2022 6:50:10 PM.

landscapes complex, we aim to untangle the effects between the two.

In this manuscript we study optical binding of large numbers of particles ($N > 20$) free to move in three-dimensional space. We assess which features of the assembly can be described by pairwise interactions verses features which emerge from higher-order effects. By comparing strong and weak scatterers, we share new insights on the relationship between refractive index, scattering strength, non-conservative forces, and non-linear optical binding. We present observations of unexpected emergent driven behaviors which appear to manifest from the deviation from pairwise forces. We also use the coupled dipole method (CDM),[27,28] also known as the discrete dipole approximation (DDA), to explain the origin of these effects.

2 Experimental design

2.1 Experimental parameters

There are a number of relevant parameters which can alter how an object scatters light and consequentially alter the properties of optical binding interactions. In practice, the most important quantities are the size parameter, ka, and the relative refractive index $m = n_p/n_0$ (where k is the wavenumber of the incident field in the background medium, a is the particle radius, and n_p/n_0 is the particle/background medium index of refraction).

Tuning the parameters will not necessarily yield linear responses, which is why we must be careful about generalizing optical binding behavior. For instance, the size parameter alone can span three different regimes: the Rayleigh limit, $ka \ll 1$, the ray-optics limit, $ka \gg 1$, and the Mie scattering regime, $ka \sim 1$, each of which are separated by drastically different assumptions including the relevance of multiple scattering, scattering modes, and how the strength of the forces scale. Our current study is focused in the Mie regime.

The relative refractive index, m, affects the scattering strength of a single particle, and so modulates the importance of multiple-scattering events.[29] We use this study as an opportunity to contrast the behaviors of strong and weak scatterers. We perform a side-by-side analysis of two commonly available colloidal microspheres which differ in refractive index. We refer to these as high-index particles (HIPs, $m = 1.2$, made of polystyrene) and low-index particles (LIPs, $m = 1.1$, made of SiO_2).

Unique to field-driven self-organization, direction and geometry become particularly important. Because optical scattering is directional, optical binding is an interaction which breaks symmetry along the axis of the field direction. As a result, experimental and numerical studies have often focused on either two distinct optical binding geometries: lateral[11,14–16,18,30] and longitudinal[17,20,31–33] optical binding. Lateral optical binding describes binding that occurs between particles with a displacement perpendicular to the direction of propagation, $\hat{k}$, while longitudinal optical binding describes binding of particles displaced along $\hat{k}$. In the current study, we implement a novel experimental approach to present the self-organization of many particles free to interact in all directions. We believe this configuration is particularly illuminating for understanding potential bulk behaviors.

Finally, previous studies have focused on how the stability of optically bound matter is affected by damping conditions[14,18] suggesting that the low damping can lead to instabilities due to the systems inability to remove energy. Because we use sub-micron particles suspended in a fluid, our study is in an over-damped regime. Our estimated Reynold's number is on the order of $Re = 10^{-6}$ (assuming 500 nm diameter particles in water with a characteristic velocity of 1 μm s^{-1}).

2.2 Optical setup

The experiments are performed on a custom designed inverted microscope (Fig. 1a). Two Gaussian beams (λ = 532 nm in vacuum, or 400 nm in solution) are aligned and focused through the sample tube to generate a counter-propagating crossed polarized optical field ($w_0 = 27.0 \pm 0.3$ μm). The polarizations of each of the two beams can be adjusted individually which allows us to switch between a counter-propagating standing wave and a crossed polarized configuration. In this specific setup, a portion of beam power is redirected back towards the laser source which is removed using an optical isolator placed between the laser head and the beam splitter. The final focusing of the beam allows us to further modulate the beam power density. The orientation of the beam through the sample is at an angle of approximately $\phi_g = 45^\circ$ through the glass layers and $\phi = 36^\circ$ through the water. We achieve total-internal reflection at the glass–air interface at the bottom surface of the coverslip depicted in Fig. 1c. The sample tube depth is 10 ± 1 μm. We collect 3-dimensional video microscopy data using a combination of a microscope objective (40×, NA = 0.75) and an electronically tunable lens (ETL). The scanning of the ETL is synchronized with the imaging camera acquisition to capture 10 volumes per second with 50 frames per volume. By adjusting the focal length of the ETL, one can adjust the z-depth of the imaging plane shown in Fig. 1c. By driving the ETL approximately 6% of its full range, we scan more than the full 10 μm of the depth of the sample. The signal output to the ETL is in the form of a periodic sawtooth pattern (driven at 10 Hz) which increases linearly for 70% of the total period and quickly decreases linearly for the remaining 30%. As such, the first 70% of the period is used to create the full volume. The 3D scanning method gave us a spatial resolution of 0.8 μm per pixel in the z-direction and a time resolution of 10 Hz which was sufficient to reliably locate particles within the volume.

The colloidal particles in the sample exhibit only Brownian motion until they enter the beam region. Particles that diffuse into the region remain confined within the Gaussian beam but can move thermally in all 3-dimensions within the area of confinement. Radiation pressure forces, which can be a strong optical force in the direction of the field propagation,[29] are carefully balanced by the two counter-propagating beams. As nearby colloids drift into the beam, the density of the particles increase slowly. While there is no direct control to stop diffusive colloids from drifting into the beam, the variability in the number

Published on 31 May 2022. Downloaded by University of California - Merced on 9/2/2022 6:50:10 PM.

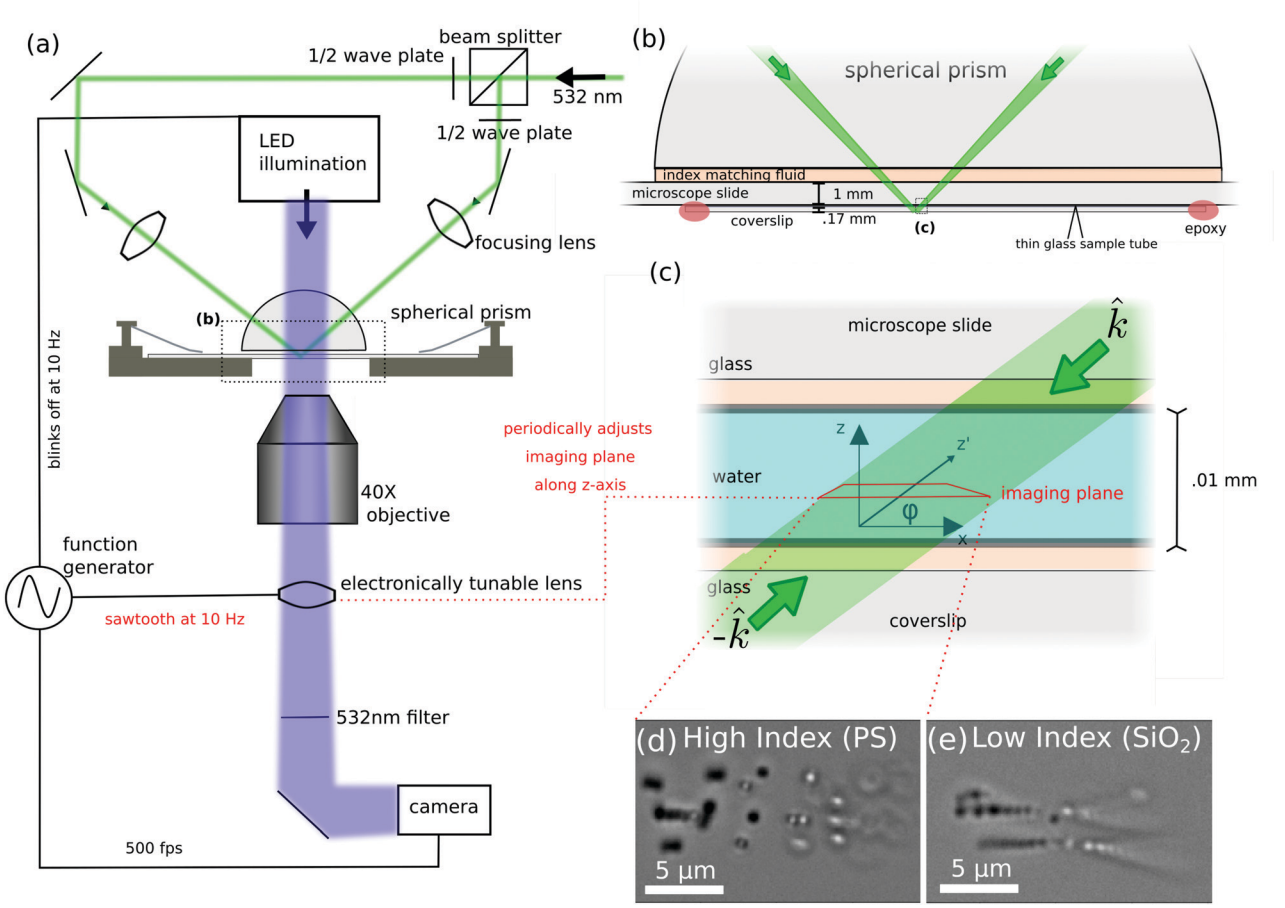

Fig. 1 (a) Experimental setup. The laser beam is split into two paths that are aligned to counter propagate through the colloidal sample. Both beams are adjusted so that they are totally internally reflected at the bottom surface of the coverslip. The polarization and incident angle of each beam can be adjusted individually by rotating the 1/2 wave plate in each path. The camera, electronically tunable lens, and illumination source are all synchronized to a wave-function generator for the acquisition of 3-dimensional videos. (b) A closer view of the spherical prism and sample at a relatively accurate scale. Here we can observe how both beams are propagated through the various layers and are aligned such that they are counter-propagating and focused within the thin glass sample tube. (c) Depth profile of sample cell, we define z-axis as direction along the sample depth and k as the axis corresponding to the beam propagation axis. The imaging plane is shifted along the z-axis by the electronically tunable lens. (d) Image of HIPs in the optical field. The image is a single slice of a 3-dimensional z-stack of images. From the specific xy-plane, the different z-positions of the particles are made obvious by the distortion of particles out of focus. In general, we can observe that the particles tend to increase height as you move along the x-axis. (e) Image of LIPs in the optical field. The image is a single slice of a 3-dimensional z-stack of images. From the specific xy-plane, the various positions along the z-axis can be seen by the distortion of particles out of focus. In general, it is observed that the particles tend to increase height as you move along the x-axis.

of particles over the entire 2 min of observation are between 1 and 5 particles ($\sim$3–7% of total particles).

The light intensity is a parameter which plays a linear role in the strength of the optical binding force and can be tuned quite easily. For the current study, we adjust the peak light intensity of the Gaussian beam up to $\sim$2.5 mW μm^{-2}. For the numerical simulations we use a reference intensity of I_0 = 1 mW μm^{-2}. Subsequently we define a reference force, F_0, which is the total optical momentum impinging on a single particle in a plane wave of intensity I_0:

$$F_0 = \frac{I_0 \pi r^2}{c}, \quad (1)$$

where r is the radius of the particle and c is the speed of light. The value approximately 650 fN for 500 nm diameter particles. It is also useful to compare this to thermal excitation. For an order of magnitude estimate of how the thermal activity compares to the strength of the optical forces in the experiment, we can convert the thermal energy, k_bT, to an equivalent force by including a length scale. Given that the optical binding force has spatial oscillations with the wavelength of the incoming light, the approximate scale of the equivalent thermal force is given by $F_T \sim k_bT/\lambda \sim 10$ fN.

We performed a numerical analysis to predict suitable light intensity and particle parameters which should allow us to observe optical binding effects (Fig. 2). By comparing the scaling of optical forces – including binding – with an estimated force of thermal excitation, we show that the size parameter is important in determining the strength of optical binding effects relative to thermal motion. The particles used in this study have a size parameter of ka = 4; as can be seen in Fig. 2 power density of 1 mW μm^{-2} should ensure that all

 This journal is © The Royal Society of Chemistry 2022

Published on 31 May 2022. Downloaded by University of California - Merced on 9/2/2022 6:50:10 PM.

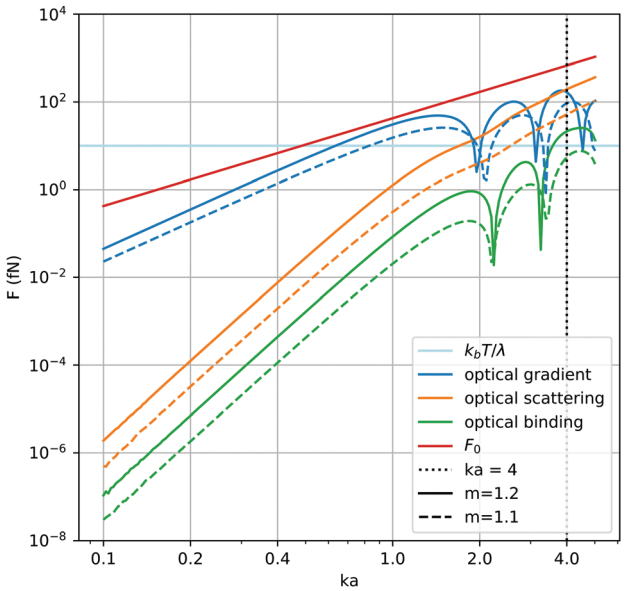

Fig. 2 Strength of optical forces for a range of size-parameters (ka). The optical gradient force (blue) was numerically simulated by placing a single particle in a node of a standing wave, the optical scattering force (orange) was numerically simulated by placing a single particle in a propagating plane-wave. The optical binding force was obtained by placing two particles laterally in a counter-propagating field at a separation of 2λ. The reference force, F_0, is also plotted. In all simulations we assume a light intensity of 1 mW μm^{-2}.

optical forces are comparable to or larger than the effective thermal forces.

Potentially more important than the strength of the force is the nature of the interaction. We note that the optical binding force is a combination of second-order gradient and scattering forces. In Fig. 2 we plot the relative strength of first-order gradient and scattering forces for HIPs and LIPs to approximate their relative contributions to the binding force. We show here that the size parameter, ka, has a strong effect on the relative balance of scattering and gradient forces, thus we draw a distinction between recent studies done on dielectric nanoparticles.[25] Note that the optical binding force is computed only for a pair of particles spaced by 2λ; for larger numbers of closely spaced particles it can be 1–2 orders of magnitude stronger. We observe for $ka = 4$ that the HIPs have a strong scattering force response, relative to the gradient force. Because scattering forces are generally non-conservative, we expect that it is the stronger presence of scattering forces in optical binding for the HIPs that give them a more dynamic self-organization behavior as opposed to the LIPs.

2.3 Sample preparation

Colloidal samples are diluted in water ($\sim$0.01 w/v%) and placed into thin rectangular Borosilicate tubes (100 μm wide × 10 μm thick × 50 mm long) purchased from VitroCom. We performed experiments with polystyrene ('HIPs', diameter d = 518 ± 10 nm, relative index m = 1.20 [34,35]) and silicon dioxide ('LIPs', diameter d = 518 ± 20 nm, relative index m = 1.10 [35,36]) purchased from microParticles GmbH. In the experiments, the number of colloidal particles are in the range of 30–50 for HIP experiments and 40–100 for the LIP experiments. We found that LIPs were more readily collected into the beam, resulting in higher effective particle densities compared to the HIPs even when the initial density is the same. The tubes allow us to keep a precise sample depth of 10 ± 1 μm. This tube depth is important for confining particles to a range in the z-direction. The tubes are coated with index matching fluid and placed in-between a coverslip and microscope slide. Finally, the coverslip is glued to the microscope slide, using UV curable Epoxy (Norland Optical Adhesive NOA61), which seals the tube and index matching fluid. The samples are fixed onto the Mad City Labs – RM21 microscopy base allowing for micro-precision movement of the sample in the x–y plane.

3 Results

3.1 Observations of self-organization behavior

Optical binding effects are immediately apparent between particles within the beam region. For instance, spatial ordering is immediately observable within the beam area – effects which can be enhanced by increasing the light intensity. The most apparent feature is the generation of multiple chains of particles aligned along the beam propagation direction (Fig. 1c). Once collected into a chain, particles within the chain can be observed to move collectively together within the beam region. The density of particles is large enough to observe the formation of multiple chains at a time.

Other features of the formed structures arise on further examination. For instance, the HIPs are found to self-organize into extended chains which extend along the sample depth-or-small clusters of typically 3–5 particles long. Both HIP structures can be observed in Fig. 1c and ESI,† Movie S1. Unlike the HIPs, the LIPs tend to form extremely long and close packed chains of particles (rods) (ESI,† Movie S2). Two LIP rods can be observed in Fig. 1d. We note that because the chains extend along the entire available depth of the sample, that the sample depth plays a relevant role as a boundary for the system.

3.2 Comparing observations to two-body forces

To understand the dominating interactions which are leading to the general behavior of both systems, we numerically generated two-body force maps for the two particle types (Fig. 3a and b). The force maps were created using a CDM based simulation[27,28] (see ESI,† for details). Comparing force maps for HIP (m = 1.2) and LIP (m = 1.1) particles reveals surprisingly little difference, apart from the overall strength. The strength differences can be observed in Fig. 2 by comparing how the optical forces are generally stronger for HIPs. The strength can be found to scale approximately like the reflectivity of a dielectric plane, which scales like $\sim (m-1)^2$.

Despite this, the two-body force maps can be used to describe some of the overall structures observed in the system. The long range alignment along the beam propagation for the

Published on 31 May 2022. Downloaded by University of California - Merced on 9/2/2022 6:50:10 PM.

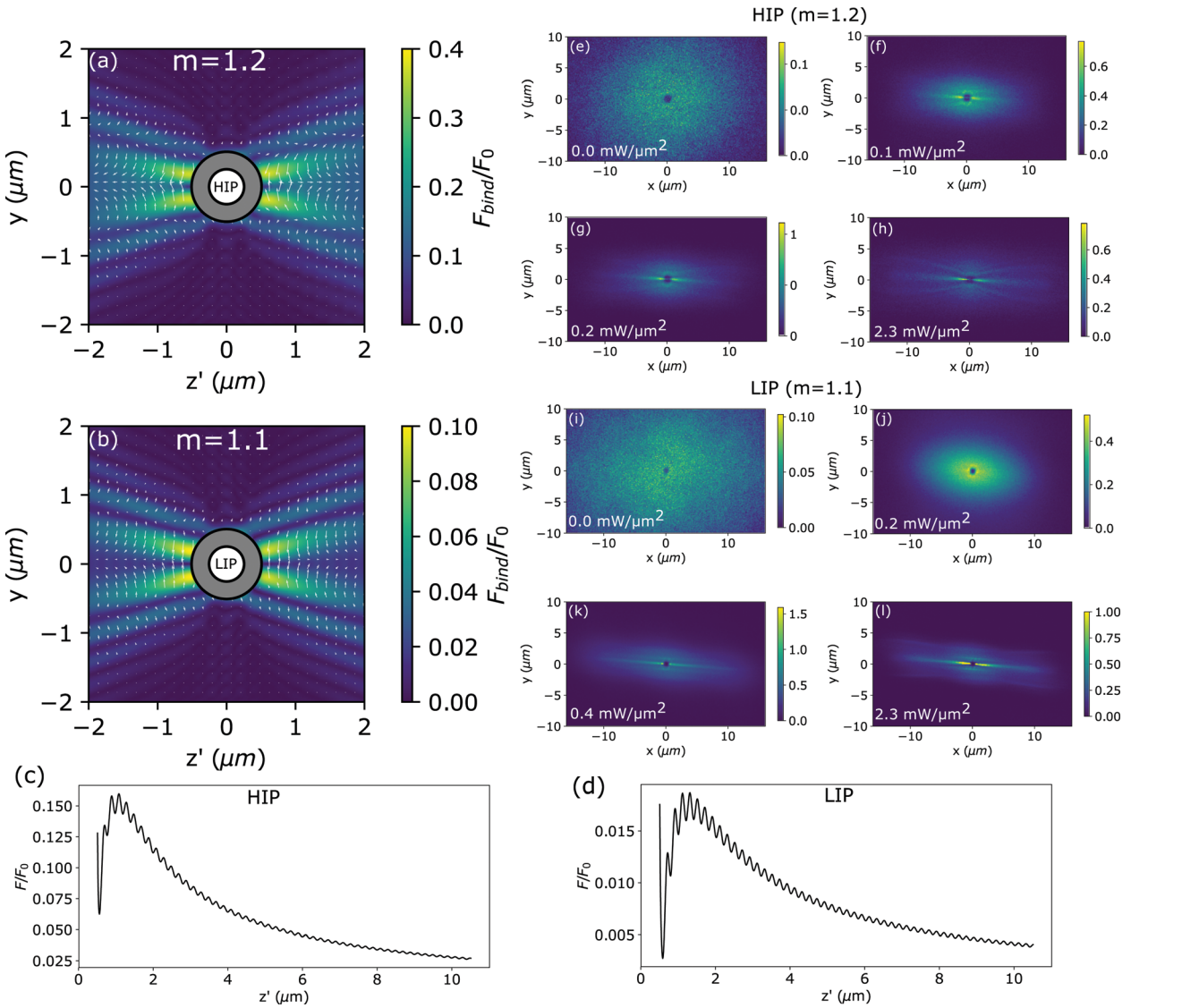

Fig. 3 (a and b) Two-body force map of optical binding forces for HIPs and LIPs (ka= 4) placed in counter-propagating crossed-polarized plane wave (λ = 0.4m in solution) propagating in the $+k = +z'$ and $-k = -z'$ direction. Maps are obtained by placing two particles in a CDM simulation and calculating the force applied on each particle at various displacements which fill the map space. The forces are provided in a unit-less scale normalized by the reference force, F_0, described by the single scattering force on a single particle of the same size and material. The direction of the arrows represent the direction of the force, while the size represents the relative strength. The white region at the center of the plots represents the particles, while the grey region around it is the excluded volume (*i.e.* particles placed at these separations would overlap). (c) The optical binding force along the axis of propagation for an extended range for two HIPs. (d) The optical binding force along the axis of propagation for an extended range for two LIPs. (e–h) 2D pair-correlation functions for HIPs in the x–y plane at various light intensities. (i–l) 2D pair-correlation functions for LIPs in the x–y plane at various light intensities. The color bar in the pair-correlation functions gives the 2D probability density of the particles, and has units of μm^{-2}.

HIPs and LIPs are qualitatively consistent with the two-body force maps (Fig. 3a and b), which suggest strong forces can tend to pull particles onto the axis of propagation ($\hat{k}$). The $\hat{k}$ axis, as shown in Fig. 1c is rotated 54 from z. For comparison, we approximate the energy $F_0\lambda \sim 65k_bT$, thus the HIPs can experience $\sim 20k_bT$ of energy keeping them aligned in the k axis in the beam at 1 mW μm^{-2}. The LIPs experience $\sim 5k_bT$ at 1 mW μm^{-2}.

The HIPs force-map shows a repulsive force between particles that are aligned along the field propagation (Fig. 3a). This fits with the observation of HIPs forming extended particle chains (Fig. 1d), rather than tightly packing. What the force-map fails to predict for the HIPs are the presence of the smaller tightly packed HIP clusters also found in the experiment. While it is expected that we observe structures that cannot be predicted from two-body optical binding interactions, here we observe an emergence of a force which is not only strongly contributing, but can act in the opposite direction of the two-body force. For the HIPs, the two-body force is repulsive along the k axis but we observe experimentally an unexpected close-range attractive force suddenly drives particles together into small clusters.

 This journal is © The Royal Society of Chemistry 2022

Published on 31 May 2022. Downloaded by University of California - Merced on 9/2/2022 6:50:10 PM.

3.3 Pair correlation function

To map the time-averaged structure created by optical binding forces, we compute a 2D pair correlation function (2D PCF). Given all the 2D particle positions, $\vec{r}_i$, we can compute all relative displacements $\vec{\Delta}_{ij} = r_i - r_{j\neq i}$; the 2D pair correlation function is then the histogram of these displacements, averaged over all frames in the data set and normalized by the bin size (so that the result is expressed as a 2D density). The form of the PCF also gives an approximation for an effective potential through which the particles interact. We collected the data for the PCF by recording the positions of colloidal particles all located within the same weakly focused beam of light. The beam is fixed at a constant light intensity for a duration of 2 min during which we collected 3-dimensional imaging data. 3-dimensional volumes were used to locate particles over the entire 10 m in depth. However, as the optical configuration results in poor resolution in z, we summed over the z-axis to generate the 2-dimensional plots. As such, the k-axis is projected along the x-axis. The particles were located using the *trackpy* implementation of Crocker and Grier.[37,38] While the particle speeds and dense particle clustering made it challenging to track particles through time, we found that the algorithms were quite efficient at locating particles within a frame. We found relatively low fluctuations in the total number of particles from frame to frame suggesting that the particle locating algorithms were performing consistently. Inter-particle displacements were determined by particle locations given for each time-step, thus the frequencies of each displacement over the entire run were available.

The PCF for the HIPs suggest an increase in spatial order with the increase in light intensity (Fig. 3e–h). The form of the PCF shows the dominating feature that the HIPs tend to align along the beam propagation. At higher light intensities, $I >$ 1 mW μm^{-2}, multiple lines off-axis begin to appear. This not only suggests that particles are interacting to form long range structures, but that there are optical binding interactions occurring in multiple directions within the field. For example, at high powers there is clear evidence of preferred inter-chain transverse spacing of $\sim$1 μm. This can be explained by the computed pairwise force diagrams, which have a converging force in the y direction at these separations. The two-body force maps (Fig. 3a and b) can be used to help explain the multiple off-axis lines that appear in the PCF at higher light intensities, as we can observe multiple off-axis lines in which the force arrows converge.

The 2D PCF for the LIPs are very consistent with the observation that the particles collapse into tightly bound rods (Fig. 3i–l). One feature that becomes prominent are secondary off-axis lines at higher light intensities. The secondary lines are evidence of multiple rods interacting to form a long-range regular spacing over time.

3.4 Volume mean squared difference (VMSD)

We use the mean squared displacement of particles to determine their dynamic behavior. Due to high-density particle clustering and the high velocities of clusters evidenced in Fig. 5 it is difficult to reliably track individual particles through time. This is especially true for close-packed clusters, which – as we shall show later – appear to drive motion in the HIPs. Instead of attempting to directly track the particles in time, we use a proxy for the mean squared displacement by obtaining the mean squared difference between two subsequent image volumes. We found that the volume mean squared difference (VMSD) between subsequent frames gives us more consistent measures of motion while remaining highly correlated with the true mean squared displacement (details of the method are described in the ESI†). The VMSD, Δ, is given by:

$$\Delta(t) = \frac{1}{N_p(t)}\left[\sum_{i,j,k}^{\text{volume}} \left(p_{i,j,k,t} - p_{i,j,k,t-dt}\right)^2 - \Delta_0\right] \qquad (2)$$

where $p_{i,j,k,t}$ is the pixel value at a given location and time, $dt = 0.1$ is the time between frames, and Δ_0 is the background VMSD caused primarily by camera noise, and is computed for when there are no moving particles in the frame.

As shown in the ESI,† Δ is proportional to the squared particle displacement provided the particles average motion between frames is smaller to or comparable the particle size. In practice, we normalize this value relative to one obtained by turning the optical binding laser off, in which case the particles experience only Brownian motion.

The distribution average particle motion for the HIPs is provided in Fig. 4a. At lower light intensities, we find narrow distributions of the average particle motion and average values lower than what is found in a Brownian system, reflecting the fact that the particles are being confined by the optical binding forces. At higher light intensities, we find that the distributions shift to higher average values and the size of the fluctuations are greater, indicating the presence of a non-conservative driving force.

Surprisingly, comparing the pair-correlation function to the VMSD values suggests that the average motion is increasing even as the particles are becoming more ordered. This would not be expected for a conservative pairwise force; in this case ordering will result in weaker fluctuations. We do indeed observe this for lower power levels ($<$0.4 mW μm^{-2}). Above these power levels, the increasing motion suggests that we are forming collections of particles which experience additional non-conservative forces from the optical field.

We found that the behavior can be altered by aligning the polarizations of the counter-propagating beams to generate a standing wave pattern. In this configuration, the optical binding area includes multiple planes of high light intensity perpendicular the propagation axis and separated by $\lambda/2$. While the overall average motion is suppressed in the standing wave, the system is still observed to fluctuate strongly between low average motion ($\sim$0.5 $\times$ Brownian motion) and high average motion ($\sim$2.5 $\times$ Brownian motion). At the same light intensities to the previous configuration, the standing wave had the effect of dramatically suppressing the overall motion (ESI,† Movie 3).

Published on 31 May 2022. Downloaded by University of California - Merced on 9/2/2022 6:50:10 PM.

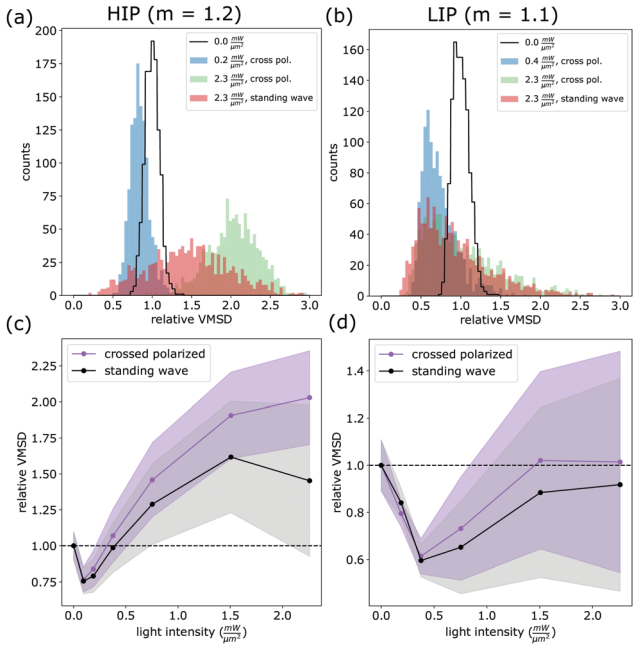

Fig. 4 (a) Distribution of relative VMSD values over 2 min duration for various intensities. For the high light intensity case (2.3 mW μm^{-2}) we share a comparative distribution of VMSD values for the same system for crossed polarizations and aligned polarizations (standing wave). (b) The average relative VMSD value over 2 minutes for various light intensities. The shaded regions represent the standard deviation in the relative VMSD values. Values over the dotted line represent the average motion of the particles greater than what would be observed when the optical binding light is turned off (*i.e.* purely Brownian motion). (c and d) The variation of relative VMSD values for various light intensities for HIPs (c) and LIPs (d). The shaded regions represent the standard deviation in the relative VMSD values. Values over the dotted line represent the average motion of the particles greater than what would be observed in a purely diffusive system.

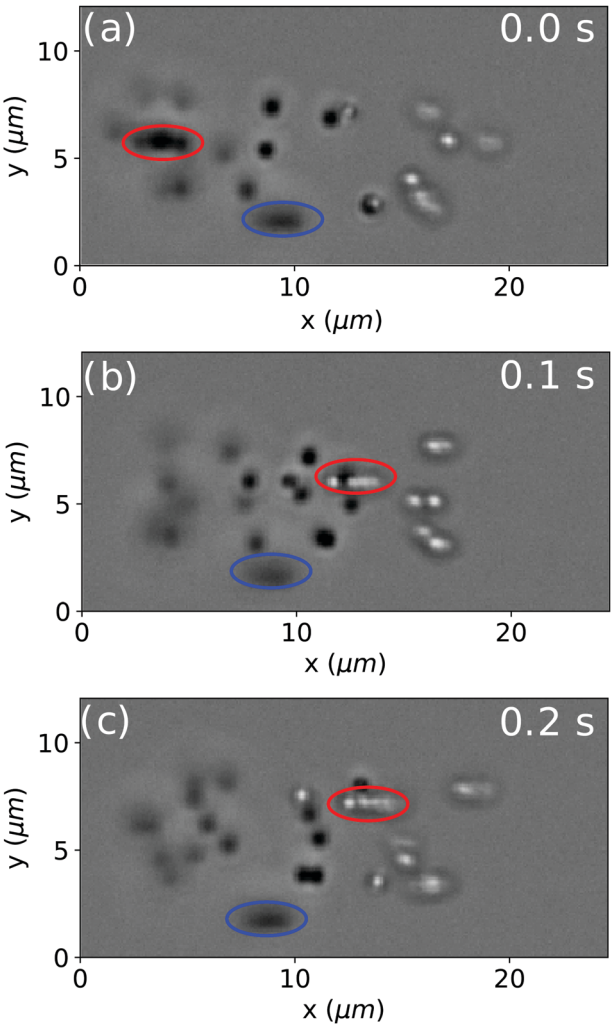

Fig. 5 (a–c) Three snapshots of the optically bound HIPs over a 0.2 s duration. Two clusters are circled: (red) cluster of 5 particles ballistically moving (>80 μm s^{-1}) through the sample and (blue) isolated cluster of 4 particles remaining relatively still.

Using the same range of intensities, the same analysis was done for the LIP system (Fig. 4b and d). At lower light intensities, we find narrow distributions of the average particle motion and mean values lower than what is found in a Brownian system. At higher light intensities, the average values do not exceed what is found in the Brownian system; however the distributions are far less Gaussian. The distribution suggests that the average motion is low with occasional rare events that lead to high motion. The LIPs in the standing wave do not show significant differences than particles in the cross-polarized counter-propagating beam.

Comparing the dynamic behavior between the HIPs and LIPs, there are clear differences between the two systems. The optical binding force when increased is shown to significantly increase the average kinetic energy of the system of HIPs. This implies that optical binding is a source of non-conservative motion that is especially present in the HIP case. We believe that non-conservative second-order scattering forces, expected to be stronger for the HIPs, is contributing to the higher overall motion. The LIPS are instead dominated by second-order gradient forces thus pack into the rod structures until density limitations require the formation of new rods. Where the standing wave generates first-order gradient forces which compete with the second-order scattering forces to suppress the overall motion, the same standing-wave does not show much of an effect on the LIPs which are already dominated by gradient forces.

3.5 Pair-correlation function difference

We see clear dynamic differences between the HIPs and LIPs; in particular, the HIPs are observed to experience higher average kinetic motion at high powers and a wider range of fluctuations of that behavior. In each case, we can use the fact that the kinetic motion does fluctuate to subset the data into high motion frames and low motion frames. Doing so gives us a method to compare particle configurations which may be correlated with driving instability in the system. To do so, we sort frames from a single video by the VMSD value which represents the average kinetic motion. We can use each subset of frames to generate PCFs for the top 30% and the bottom 30% VMSD values. Because of the wide distribution of VMSD values,

 This journal is © The Royal Society of Chemistry 2022

Published on 31 May 2022. Downloaded by University of California - Merced on 9/2/2022 6:50:10 PM.

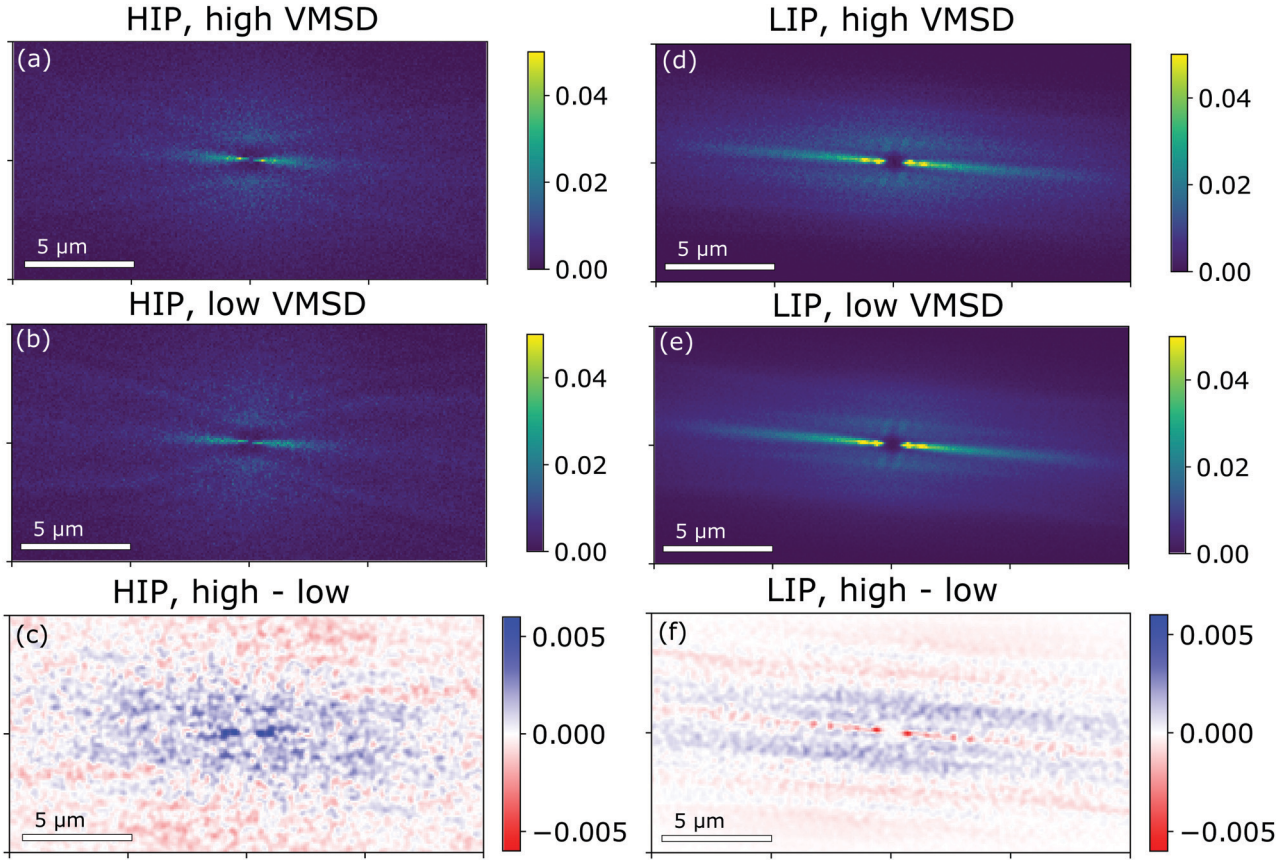

Fig. 6 (a) HIP PCF for frames with higher (top 30%) VMSD values. (b) HIP PCF for frames with lower (bottom 30%) VMSD values. (c) The difference between the high VMSD and low VMSD PCFs for HIPs. (d) LIP PCF for frames with higher (top 30%) VMSD values. (e) LIP PCF for frames with lower (bottom 30%) VMSD values. (f) The difference between the high VMSD and low VMSD PCFs for LIPs. Displacements found more often in the higher VMSD frames are positive (blue) while displacements found more often in the lower VMSD frames are negative (red). The PCFs are normalized by dividing the 2D particle density by the number of particles.

we focus on particles in a high powered (2.3 mW μm^{-2}) standing wave.

Comparing the PCFs for the high VMSD frames (Fig. 6a) *versus* the low VMSD frames (Fig. 6b) for the HIPs shows subtle differences. Primarily, we find more defined features for the low VMSD PCF. This suggest that the system fluctuates between slower moving ordered states to faster moving disordered states. Indeed, we observe sudden collapses and regeneration into order states in these optically bound systems.

Secondly, we observe that there is a higher distribution of particles in close proximity for the faster moving system. We illuminate this subtle difference by subtracting the low VMSD PCF from the high VMSD PCF shown in Fig. 6c. We propose that multiple scattering effects which are stronger when particles are at close-range could be driving the collapse of stability and increase in average kinetic motion of this system.

For the LIPs, we find that the high VMSD PCF (Fig. 6d) *versus* the low VMSD PCF (Fig. 6e) are both structurally similar. Not until taking the difference between the two as shown in Fig. 6f, do we see that there are subtle differences. For the low VMSD PCF, we observe that particles tend to be distributed among multiple lines: a single line that passes the origin and multiple off-axis lines. These lines are evidence of the self-organization into multiple rods. The center line represent displacements between particles that belong to the same rod and the off-axis lines represent displacements between particles that are located in neighboring rods. Interestingly, the differences between the high and low PCFs suggest that inter-rod distance may play a role in the average kinetic motion of this system. For instance, one can observe in Fig. 6f that the first off-axis line is closer to the center line for the higher VMSD frames.

Comparing the HIPs and the LIPs is useful for understanding how multiple scattering is affecting these systems at different scales. For the HIPs, where scattering is much stronger, we find that the presence of small clusters are generally correlated with higher kinetic motion and less structural order of the overall system. We propose that HIP clusters can be treated as an emergent species which can alter the system dynamics. On the other hand, the LIPs can generate much larger stable structures before the system fluctuates dynamically.

3.6 Pathway to cluster formation

The two-body force maps cannot describe how a cluster or rod forms; in fact, the two-body force maps suggest a weak repulsive force among particles that are aligned along the beam propagation. As a result, we believe the cluster formation can

Published on 31 May 2022. Downloaded by University of California - Merced on 9/2/2022 6:50:10 PM.

only be explained by considering a complete N-body force which we compute using the CDM.

We find numerically that when the separation between aligned particles is sufficiently large ($\gtrsim 0.25$ μm) the total force is always repulsive for HIP chains and increases in strength with the number of particles (Fig. 7a). This suggests that a chain of particles aligned along the propagation axis should remain spread apart. This is consistent with some of the structures found in the experiment: the lower density HIP chains are often found extending from the lower to upper boundary of the sample. The strong repulsion at long range could also act as a barrier to cluster formation at very high light intensity and low particle density. The trend is similar for LIP chains (Fig. 7b).

At smaller distances, we observe a decrease in repulsive strength for all HIP chains. For HIP chains of more than 3 particles, we observe an overall change in sign of the force (Fig. 7a). This result suggests that the two-body repulsive force (Fig. 3a) dominates as long as the particles are far away; however, when many HIPs become in close range, N-body forces are strong enough to overcome two-body repulsion and switch the sign of the force entirely.

The same analysis of the LIP chains of particles shows a similar reduction of the repulsive force at shorter distances; however, an attractive force does not appear until the number of particles exceeds $N = 14$ (Fig. 7b). The initial reduction of the force, even at small N, is indicative of the presence of non-pairwise forces; however the effects are clearly weaker in comparison to the HIPs.

The numerical results provide a potential pathway to the previously unexpected formation of clusters. The results also highlight the unique nature of the N-body optical binding forces. These effects are shown to be comparatively much stronger for the HIPs. This supports the hypothesis that a major factor driving the differences in behavior between the HIP and LIP systems is a stronger presence of N-body forces due to the higher scattering strength of HIPs.

3.7 Non-conservative forces on clusters

We simulated the effects of a particle cluster as it grows in size and interacts with neighboring particles. We simulate a simplified configuration of N-particle closed packed cluster in line with a single lone particle at varying distance. We then compute the total force on the clustered particles, F_c, as well as the force on the lone particle, F_p. To compare the relative presence of conservative and non-conservative forces, we use the following quantity:

$$\gamma = \frac{|F_c + F_p|}{|F_c - F_p|} \tag{3}$$

If the forces are equal and opposite – indicating a conservative interaction – we will obtain $\gamma = 0$. In contrast, if the forces are equal but in the same direction, this would be indicative of a system which would be driven ($\gamma \to \infty$).

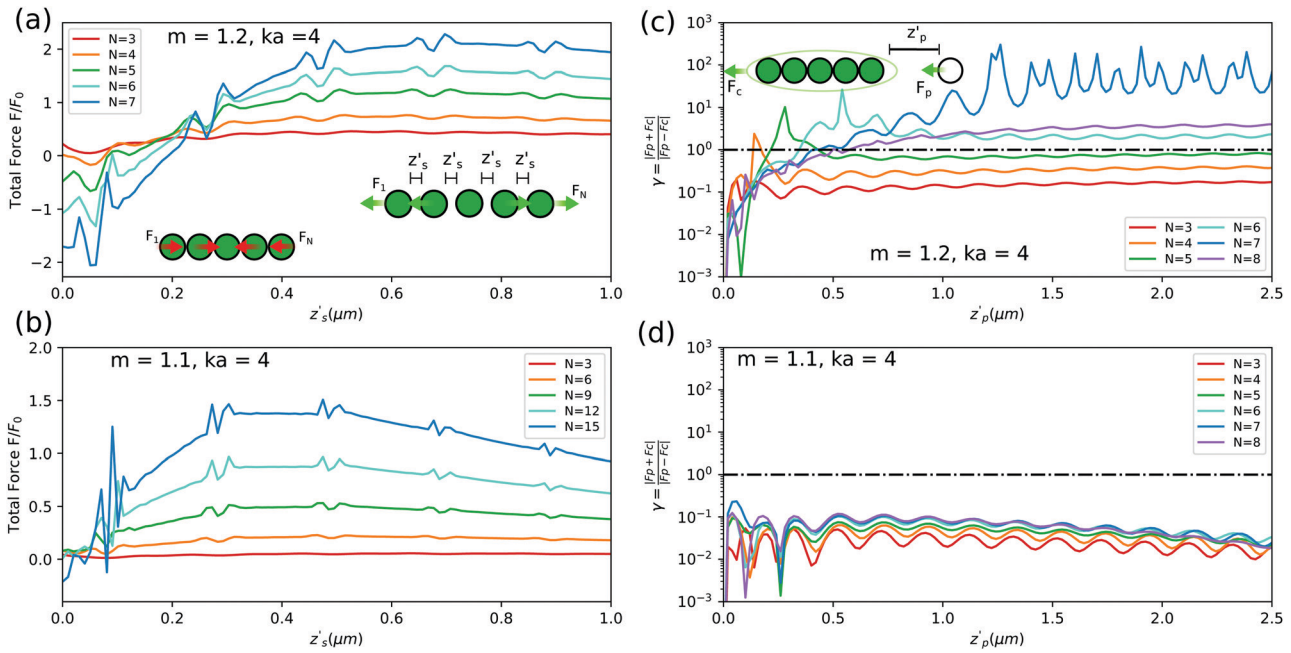

Fig. 7 (a and b) 1-Dimensional simulation of forces on particle chains. Particles are placed into a equidistant configuration aligned with the beam axis of propagation ($k = z'$) with inter-particle distance, $z_{s'}$. At each inter-particle spacing, the total outward force is calculated. A positive force represents a net-force pushing particles away from each other while a negative force represents a net-force in which particles are attracted. We performed the simulation for (a) HIPs ($m = 1.2$, $ka = 4$) and (b) LIPs ($m = 1.1$, $ka = 4$) for various cluster sizes (N) (c and d) 1-dimensional simulation of forces between clusters and neighboring particles. A cluster of N touching spheres is aligned along the axis of propagation with a single particle and the absolute sum over the absolute difference of force on the cluster and the force on the particle are plotted for various particle-cluster spacings, z'_p. Simulations were performed for (c) HIP ($m = 1.2$, $ka = 4$) and (d) LIP ($m = 1.1$, $ka = 4$) particles.

 This journal is © The Royal Society of Chemistry 2022

Published on 31 May 2022. Downloaded by University of California - Merced on 9/2/2022 6:50:10 PM.

Observing γ for the interaction between the HIP cluster and particle, we find that the value increases exponentially as the cluster size increases from 2–6 particles (Fig. 7c). At $\gamma > 1$ the force between the cluster and the particle are in the same direction, while for $\gamma \gg 1$ the forces are highly non-conservative.

For HIPs, there are configurations which could lead to unidirectional interactions first appearing for clusters of size 4. For clusters of sizes $N > 5$ particles, we find that $\gamma > 1$ at long ranges. This result is in good agreement with our observations of driven HIP clusters. At certain cluster sizes, non-conservative forces appear to allow clusters of particles to propel in an otherwise symmetric initial field. Despite the particles being identical in the simulation, the cluster-particle interaction adds an asymmetry which can drive the system into unidirectional motion in some cases. Here we study a limited set of configurations due to their common observable presence in the experimental data; however, we expect there are a number of alternative configurations that can also exhibit highly propelled motion. We expect that these strongly non-conservative interactions are cause for the increased average motion in the high light intensity binding experiments (Fig. 4(a and b)).

For a similar set of cluster sizes in the LIP case, we find $\gamma < 0.1$ regardless of cluster size (Fig. 7d). Indeed, we observed in the experiments that LIPs can build themselves into extremely long rods without exhibiting strongly non-conservative responses at small cluster sizes, as we found for the HIPs. It is likely that non-conservative forces won't have a strong presence for LIPs until they've assembled into elongated rods for which we do observe fluctuations in the VMSD values.

4 Conclusion

Optical binding of many particles in 3D gives rise to complex behavior that can not be predicted from two-body interactions alone. A simplified view of the interaction does, however, predict some features of the resulting structures: in particular the formation of extended chains of particles along the axis of light propagation. However, comparing low to high index particles – whose two-body interaction is nearly identical apart from overall strength – already demonstrates differences that must arise from *N*-body interactions. Our results stress how the relative strength of gradient and scattering forces play a role in these systems. For instance, $ka \ll 1$ particles have been shown to experience interesting conservative interactions on complex potential landscapes; however exploring larger *ka* affords the capability of controlling non-negligible contributions of non-conservative binding forces. It is at this size regime that we are able to find considerable differences between the LIPs and HIPs. In particular, the lower index particles form close packed (or nearly closed packed) chains, while the higher index particles are aligned with the beam, but usually spaced out by several particle diameters. More strikingly, the dynamic behavior of these particles demonstrates effects that can only be explained by considering non-conservative *N*-body interactions. This is most dramatically demonstrated by the temporary formation of close-packed clusters of 4–5 high index particles, which appear to drive an instability of the system as a whole.

Our results suggest that although optical binding can be used to guide the self-organization of colloidal particles, the effects of *N*-body forces are critical for the assembly of many-particle systems when their scattering strength is sufficiently strong. Notably, this is distinct from nano-particle assembly with optical binding, in which pairwise forces are generally a good approximation.[23] Potentially, this more complex force landscape offer new possibilities: with proper system design these forces could be used to promote or evade specific configurations or produce driven arrangements with dynamic behavior. Unfortunately, predicting the behavior of large scale optically bound systems remains a difficult task without a quick and accurate method of computing the forces for a fully coupled *N*-body system. Efforts on this front can be aided by further experimentation which can validate assumptions regarding *N*-body and non-conservative effects over a larger parameter space than the current study.

Conflicts of interest

There are no conflicts to declare.

Acknowledgements

We would like to acknowledge funding from the National Science Foundation (NSF grant 2046261) and the Hellman Fellows Fund.

Notes and references

1 G. M. Whitesides and B. Grzybowski, *Science*, 2002, **295**, 2418–2421.
2 B. A. Grzybowski, C. E. Wilmer, J. Kim, K. P. Browne and K. J. M. Bishop, *Soft Matter*, 2009, **5**, 1110.
3 F. Ginot, I. Theurkauff, F. Detcheverry, C. Ybert and C. Cottin-Bizonne, *Nat. Commun.*, 2018, **9**, 696.
4 A. Wang, W. Shi, J. Huang and Y. Yan, *Soft Matter*, 2015, **12**, 337–357.
5 J. R. Howse, R. A. L. Jones, A. J. Ryan, T. Gough, R. Vafabakhsh and R. Golestanian, *Phys. Rev. Lett.*, 2007, **99**, 048102.
6 B. A. Grzybowski, H. A. Stone and G. M. Whitesides, *Nature*, 2000, **405**, 1033–1036.
7 B. A. Grzybowski, H. A. Stone and G. M. Whitesides, *Proc. Natl. Acad. Sci. U. S. A.*, 2002, **99**, 4147–4151.
8 G. Kokot, G. V. Kolmakov, I. S. Aranson and A. Snezhko, *Sci. Rep.*, 2017, **7**, 14726.
9 P. Tierno, R. Golestanian, I. Pagonabarraga and F. Sagués, *Phys. Rev. Lett.*, 2008, **101**, 218304.
10 A. Snezhko and I. S. Aranson, *Nat. Mater.*, 2011, **10**, 698–703.
11 M. M. Burns, J.-M. Fournier and J. A. Golovchenko, *Phys. Rev. Lett.*, 1989, **63**, 1233–1236.

Published on 31 May 2022. Downloaded by University of California - Merced on 9/2/2022 6:50:10 PM.

12 T. Thirunamachandran, *Mol. Phys.*, 1980, **40**, 393–399.
13 J. Bai, Z.-S. Wu and C.-X. Ge, 12th International Symposium on Antennas, Propagation and EM Theory (ISAPE), 2018, pp. 1–3.
14 X. Li, Y. Liu, Z. Lin, J. Ng and C. T. Chan, *Nat. Commun.*, 2021, **12**, 6597.
15 F. Dapasse and J. M. Vigoureux, *J. Phys. D: Appl. Phys.*, 1994, **27**, 914–919.
16 S. K. Mohanty, J. T. Andrews and P. K. Gupta, *Opt. Express*, 2004, **12**, 2746–2753.
17 S. A. Tatarkova, A. E. Carruthers and K. Dholakia, *Phys. Rev. Lett.*, 2002, **89**, 283901.
18 J. Ng, Z. F. Lin, C. T. Chan and P. Sheng, *Phys. Rev. B: Condens. Matter Mater. Phys.*, 2005, **72**, 085130.
19 N. K. Metzger, K. Dholakia and E. M. Wright, *Phys. Rev. Lett.*, 2006, **96**, 068102.
20 V. Karásek, T. Čižmár, O. Brzobohatý, P. Zemánek, V. Garcés-Chávez and K. Dholakia, *Phys. Rev. Lett.*, 2008, **101**, 143601.
21 K. Dholakia and P. Zemánek, *Rev. Mod. Phys.*, 2010, **82**, 1767–1791.
22 J. Rodríguez, L. C. Dávila Romero and D. L. Andrews, *Phys. Rev. A: At., Mol., Opt. Phys.*, 2008, **78**, 043805.
23 K. A. Forbes, D. S. Bradshaw and D. L. Andrews, *Nanophotonics*, 2020, **9**, 1–17.
24 F. Nan, F. Han, N. F. Scherer and Z. Yan, *Adv. Mater.*, 2018, **30**, 1803238.
25 O. Brzobohatý, L. Chvátal, M. Šiler and P. Zemánek, *Opt. Express*, 2020, **28**, 37700.
26 Z. Yan, S. K. Gray and N. F. Scherer, *Nat. Commun.*, 2014, **5**, 3751.
27 B. T. Draine and P. J. Flatau, *JOSA A*, 1994, **11**, 1491–1499.
28 A. G. Hoekstra, M. Frijlink, L. B. F. M. Waters and P. M. A. Sloot, *JOSA A*, 2001, **18**, 1944–1953.
29 A. Ashkin, J. M. Dziedzic, J. E. Bjorkholm and S. Chu, *Opt. Lett.*, 1986, **11**, 288–290.
30 M.-T. Wei, J. Ng, C. T. Chan and H. D. Ou-Yang, *Sci. Rep.*, 2016, **6**, 38883.
31 V. Karásek, K. Dholakia and P. Zemánek, *Appl. Phys. B: Lasers Opt.*, 2006, **84**, 149–156.
32 V. Karásek, O. Brzobohatý and P. Zemánek, *J. Opt. A: Pure Appl. Opt.*, 2009, **11**, 034009.
33 W. Singer, M. Frick, S. Bernet and M. Ritsch-Marte, *JOSA B*, 2003, **20**, 1568–1574.
34 X. Zhang, J. Qiu, J. Qiu, J. Qiu, X. Li, X. Li, J. Zhao, J. Zhao, L. Liu and L. Liu, *Appl. Opt.*, 2020, **59**, 2337–2344.
35 G. M. Hale and M. R. Querry, *Appl. Opt.*, 1973, **12**, 555–563.
36 I. H. Malitson, *JOSA*, 1965, **55**, 1205–1209.
37 J. C. Crocker and D. G. Grier, *J. Colloid Interface Sci.*, 1996, **179**, 298–310.
38 D. Allan, T. Caswell, N. Keim and C. van der Wel, *trackpy: Trackpy v0.3.0*, 2015, **https://zenodo.org/record/34028**.

 This journal is © The Royal Society of Chemistry 2022